THE INFLUENCE OF OXYGEN ON THE HER CATALYTIC ACTIVITY OF ELECTRODEPOSITED MOO_XS_Y ELECTROCATALYSTS AND PROGRESS OF 3D CARBON TUBE SUPPORTED MOO_XS_Y CATALYSTS TO ENABLE LONG-TERM HUMAN ACTIVITY ON MARS

Lee Kendall[1], Amir Chamaani[1], Zachary Piontkowski[2], Thomas Beechem[2], Mackenzie Ridley[1], Elizabeth Opila[1], Giovanni Zangari[1], Stephen McDonnell[1]

[1]Department of Materials Science and Engineering, University of Virginia, 395 McCormick Road, Charlottesville, VA 22903, United States

[2]Center for Integrated Nanotechnologies, Sandia National Laboratories, 1515 Eubank Boulevard, Albuquerque, NM 87123, United States

Abstract

Amorphous, polymeric molybdenum sulfide has attracted significant attention as non-platinum group electrocatalysts for the hydrogen evolution reaction (HER). To elucidate the influence of oxygen incorporation on molybdenum sulfide catalysts, MoO_xS_y electrocatalysts were synthesized via a potentiostatic electrodeposition method. The presence of oxygen and the associated molybdenum oxidation state were modified by post-synthesis treatments of air exposure, annealing in inert atmosphere, and annealing in a sulfur flux. The as-deposited sample exhibited the best performance, requiring only 171 mV to reach a cathodic current density of 10 mA/cm^2. While the modified films exhibited worse HER performance compared to the as deposited sample, by utilizing extensive X-ray photoelectron spectroscopy studies, the importance of the Mo^{5+} oxidation state was highlighted while identifying a previously unreported transition state between Mo^{4+} and Mo^{5+}, deemed Mo*. Additionally, to further increase the performance of the films, a 3D conductive substrate of carbon paper (CP)/carbon tubes (CT) was synthesized. While the CP/CT substrate has not been successfully synthesized, early results show that the attempts have increased the overall performance, lending credence to the approach that has the potential to rival state-of-the-art water splitting catalysts.

1. Introduction

This work was motivated by the need to develop extremely robust and effective methods for extending human activity on Mars due to the increasing drive to further explore and eventually send humans to Mars(*1*). As the surface of Mars is unsuitable for extended human activity, future explorations will require a steady source of oxygen and energy, both for daily needs as well as for returning to Earth. Among technologies available on Mars, solar energy is by far the largest available resource(*2*). An attractive solution to both the problems of energy production and oxygen generation would be to store the solar energy in the form of chemical bonds, H_2 and O_2, which later could be used for energy production and human consumption.

Photoelectrochemical (PEC) water splitting and electrolysis are such processes and substantial efforts have been invested in the pursuit of photoactive and durable semiconductor materials (*3–12*). The free energy change for one molecule of H_2O to H_2 and ½ O_2 under standard conditions generates a ΔG of 237.2 kJ/mol which corresponds to ΔE^o = 1.23 V per transferred electron. To utilize semiconductors and be able to drive the reaction with light, the semiconductor must absorb light with energies > 1.23 eV and convert this energy into the bonds of H_2 and O_2. This process must generate two electron – hole pairs per molecule of H_2 or four electron – hole pairs per molecule of O_2. The state-of-the-art catalysts for the hydrogen evolution reaction (HER) and oxygen evolution reaction

(OER) are Pt and RuO_2, respectively, although poor durability and long-term availability are a concern due to their scarcity and associated high costs. As such, non-noble transition-metal-based dedicated catalysts in conjunction with graphene to enhance overall conductivity for the HER and OER with commensurate performances are being explored extensively.

For this reason, alternative electrocatalysts based on naturally abundant transition metal sulfides, phosphides, nitrides, and carbides(*13–16*) are increasingly being pursued. One example is MoS_2-based catalysts, which are particularly intriguing due to their small Gibbs adsorption energy for hydrogen, $\Delta G^H_{0,ads}$(*17–20*), and thus their ability to mediate the hydrogen evolution reaction (HER). This low $\Delta G^H_{0,ads}$ is only observed along the edge planes of crystalline MoS_2, thus inherently limiting the number of active catalytic sites (*21*). Recent efforts have attempted to increase the number of active sites in MoS_2 via several approaches, such as: vertically aligned synthesis, purposeful creation of sulfur vacancies, the use of nanoparticles, or heteroatom doping (*22–30*).

Each of these approaches effectively lessens the crystalline order of the solid as a means to increase catalytic activity. Disordered MoS_2 solids therefore provide a more straightforward path to this end. For example, coordinated polymeric MoS_y chains—typically termed amorphous MoS_2 or a-MoS_2—exhibit excellent catalytic activity for HER owing to the combination of structural heterogeneity that increases catalytic site density combined with short-range atomic arrangements that enable sufficient electronic conductivity for use in electrochemical processes (*14*, *31–35*).

Despite this general understanding, the exact interplay of physical processes through which a-MoS_2 catalyzes the HER reaction remain unclear thus obscuring routes to further improvement. Tran et al. attributed the catalytically active site to the removal of the terminal sulfur ligands and the subsequent formation of M=O species(*14*). However, separate work utilized in-operando Raman spectroscopy to identify the breaking of bridging S-S bonds within the MoS_y chains as the primary site for catalytic activity(*33*, *36*). In other work, the incorporation of oxygen was shown to improve the catalytic performance(*31*). Therefore, the incorporation of oxygen increases the overall catalytic activity by either accentuating the catalytic activity of the broken bridging S-S bonds or by another means, such as acting as catalytic sites themselves. It has been hypothesized that oxygen could serve as a dopant increasing the electrical conductivity of the a-MoS_y and thus its electrochemical capability or as an additional catalytically active site(*14*, *31*). Simply put, while it is generally accepted that the presence of oxygen during the deposition of a-MoS_y is a net "win" for catalyzing HER, the exact reason for its usefulness remains the subject of debate.

In response, the catalytic performance of a-MoS_y is examined as a function of oxygen content. Practically, a-MoO_xS_y films were synthesized from separate sulfur and oxygen containing molybdenum precursors to induce oxygen incorporation of the film. This synthesis is notably different from the majority of previous electrodeposition studies as the $(MoS_4)^{2-}$ anion is synthesized in solution as per Levinas et al.'s in-depth electrochemical study(*37*). The Levinas study demonstrated superior performance, specifically lower overpotential to reach 10 mA/cm^2, than the single precursor studies. However, there was no detailed chemical analysis. Motivated by that work, we seek to understand why that synthesis route exhibits increases performance over the other routes. Additionally, the oxygen content was then varied post-synthesis by annealing a subset of the films to inert and sulfuric environments as well as an extended exposure in atmosphere (i.e., oxidation). These films were then analyzed electrochemically, and performance assessed in terms of material variation as deduced from X-ray photoelectron (XPS) and Raman spectroscopies. Together, the results highlight oxygen's role in promoting the catalytically favorable Mo^{5+} state within a-MoO_xS_y.

Following the investigation and optimization of the MoO_xS_y catalysts, the next step was growing this material on a carbon paper (CP) - carbon tube (CT) substrate. The synthesis of the carbon tubes was carried out following Wang et. al.'s chemical bath synthesis(*38*). While achieving the CTs have been an issue as seen when investigated via Scanning Electron Microscopy (SEM), we still are able to measure an appreciable improvement in the performance, demonstrating the potential for this method. While the HER performance of the CP-CT-MoO_xS_y falls short of expensive Pt electrodes, they still perform only

slightly behind state-of-the-art carbides and phosphides.

2. Experimental

Electrolyte Preparation

The molybdenum disulfide films were electrodeposited from a chemical bath containing precursors of Mo^{6+} and S^{2-} ions, based on Levinas et al. preparation(*37*). In short, the electrolyte was prepared from sodium molybdate dihydrate ($Na_2MoO_4*2H_2O$) and sodium sulfide hydrate (Na_2S*H_2O) were mixed in a ratio of Mo/S = 1/4 with molarities of 50 mM and 0.2 M, respectively. The sulfidation of molybdate ions to tetrathiomolybdate (MoS_4^{2-}) is a four-step reaction described by the equation:

$$MoO_4^{2-} + 4HS^- + 4H^+ \leftrightarrow MoS_4^{2-} + 4H_2O \quad (1)$$

The initial pH of the solution was approximately 13 and was acidified using sulfuric acid to a pH of 8. This acidification was carried out to shift the equilibrium to the reactants side so as to favor the formation of MoS_4^{2-} over other intermediates.

MoO_xS_y Electrodeposition

All electrochemical depositions were carried out using a G&G PAR Model 273A potentiostat in a standard three-electrode setup containing Pt mesh as a counter electrode and saturated Hg/Hg_2SO_4 (MSE) as the reference electrode. The substrate was a (0001)-textured polycrystalline Ru (80 nm) sputtered onto a Si wafer as the working electrode. Unless specified, all potentials are referenced to Hg/Hg_2SO_4. The Ru substrates were washed with 2-proponal and distilled water prior to deposition. The films were deposited under potentiostatic conditions at -1.5 V for 1800 seconds as longer times exhibited delamination issues.

Annealing

To vary the concentration of oxygen within the films, various different anneals were carried out in an MTI OTF-1200X tube furnace. Practically, annealing was accomplished by heating the samples to 250°C at a ramp rate of 7.5°C/minute where it was held for 60 minutes before being naturally cooled back to ambient. Oxygen content was varied by changing atmosphere in the anneal. In one case, the anneal took place in the presence of ultrahigh purity nitrogen gas. We term this case the “inert anneal.” A separate “sulfur anneal” was implemented by placing roughly 200 mg of elemental sulfur powder located 10 cm upstream of the film during the anneal, which was transported to the sample via the purge gas. Irrespective of the anneal a 45-minute purge with the same nitrogen gas was used to minimize the presence of any impurities within the furnace. These processes resulted in two samples that are referred to hereafter as “inert anneal” and “sulfur anneal”. In addition to these samples, we also investigated an as-deposited samples and an as-deposited sample that was exposed to air for several days. These are referred hereafter as “as-deposited” and “air exposed”.

Electrochemical Hydrogen Evolution

Electrochemical characterization of the prepared films for HER was performed by a three-electrode configuration using a G&G PAR Model 273A potentiostat. The MoO_xS_y, platinum mesh, and Hg/Hg_2SO_4 were used as the working, counter, and reference electrode, respectively. All experiments were carried out in fresh 0.5 M H_2SO_4 solutions at room temperature. The electrochemical potential difference between the reversible hydrogen electrode (RHE) and the reference electrode is given by $E(RHE) = E(Hg/Hg_2SO_4) + 0.64$ V. The polarization curves of HER were measured using linear sweep voltammetry (LSV) at a starting potential of open circuit potential and swept at a rate of 10 mV/sec with a cutoff current density of 40 mA/cm^2. All LSV tests were performed as quickly as possible, in order to reduce oxidation of the sample(*37*).

Carbon Tube Synthesis

The 3D conductive substrate of CP/CNTs will be synthesized using an established procedure that involves several steps(*38*).

Synthesis of Carbon Paper (CP)/ZnO NWs

The CP was first heat-treated at 500°C for 1 hour in air to increase the overall wettability. The CP was then soaked in 0.1 M $KMnO_4$ for 1 hour to form a seed layer. The seeded CP was then immersed in a bottle containing an aqueous solution containing 15 mM zinc nitrate hexahydrate, 15 mM hexamethylenetetramine, 4 mL of ammonia, and 96 mL of distilled H_2O. The bottle was then sealed tightly and placed in an oven at 90°C for 24 hours. It was then rinsed with water and dried at 80°C for 3 hours.

Synthesis of CP/ZnO NW/Polydopamine (PDA)

Following drying, the CP/ZnO NW was immersed in a solution of 18 mL ethanol, 20 mL water, and 60 mg of dopamine hydrochloride. Following, 60 mg of Tris was dissolved in 2 mL of ethanol and was added to the primary solution. After 24 hours, the substrate was taken out and rinsed with water and ethanol and was dried at 60°C for 8 hours.

Synthesis of CP/Carbon Tubes (CT)

The CP/ZnO NWs/PDA was calcinated at 800°C for 1 hour under an Ar/H_2 atmosphere. Following cooling to room temperature, the substrate was immersed in 1 M HCl for 24 hours to remove any Zn species. This was followed by water washing and drying at 80°C for 8 hours to obtain CP/CTs.

Materials Characterization

Differential Scanning Calorimetry (DSC) was carried out using a Netzsch STA449 F1 Jupiter with a SiC furnace. X-ray photoelectron spectroscopy (XPS) spectra were collected from a Scienta Omicron R3000 using monochromatic Al Kα emission with an excitation energy of 1486.7 eV and a pass energy of 50 eV. The features of the Mo 3d were deconvoluted with the doublet of $3d_{5/2}$ and $3d_{3/2}$ with the area ration of 3:2 and a binding energy difference of 3.13 eV. The spectra of the S 2p was deconvoluted with the doublet of $2p_{3/2}$ and $2p_{1/2}$ with an area ratio of 2:1 and a binding energy difference of 1.18 eV. Raman spectroscopy was collected using a Renishaw Raman instrument with a 514 nm laser excitation.

3. Results and Discussion – MoO_xS_y Catalysts for HER

Error! Reference source not found. shows the resonance Raman spectrum of amorphous, polymeric MoO_xS_y deposited on a Ru electrode at -1.5 V versus MSE. The a-MoO_xS_y material shows nearly identical Raman signatures to those reported for isolated $[Mo_3S_{13}](NH_4)_2$ clusters(*14*, *39*). The molybdenum sulfide bonds of ν(Mo-S) were found at 283-385 cm^{-1} and the ν(Mo-S_{apical}) vibrations were observed in the 450-475 cm^{-1} region while the ν(Mo-S-Mo) vibrations were observed around 425 cm^{-1}. Additionally, the bands of ν(Mo=O) and ν(Mo(=O)$_2$) vibrations were observed between 180 cm^{-1}- 215 cm^{-1}, 560 cm^{-1} in the range of 800-960 cm^{-1} (*40*). The freshly deposited film does not show strong ν(S-S)$_{terminal}$ or ν(S-S)$_{bridging}$ Raman peaks at 520 cm^{-1} or 550 cm^{-1}, respectively. This missing feature has been ascribed to unsaturated S^{2-} species as revealed by XPS(*33*). These Raman signatures are in good agreement with previous literature(*31–34*, *41–43*). It should be noted that the bands shown are drastically different from the sharp E^1_{2g} and A_{1g} peaks from bulk, crystalline MoS_2 which are obtained after annealing above the crystallization temperature of roughly 420° C as determined by DSC. We noted that when annealing at lower temperatures for extended periods of time the onset of crystallization could be detected with Raman spectroscopy. To avoid any crystallization, the samples were annealed at 250° C. The difference in the Raman spectra highlights that the electrodeposited amorphous films show structures fundamentally different from that of crystalline MoS_2(*13*, *32*, *44*). Additionally, when left in air, the features associated with Mo=O vibrations increases in intensity demonstrating that the film oxidizes over time(*14*, *40*). These results agree with the XPS findings shown in Figure 3. Both annealed samples closely resemble the as deposited spectra, however there are fine differences around 450 cm^{-1} and 530 cm^{-1}. The sulfur anneal sample exhibits enhanced intensity around 450 cm^{-1}, demonstrating an increase in the

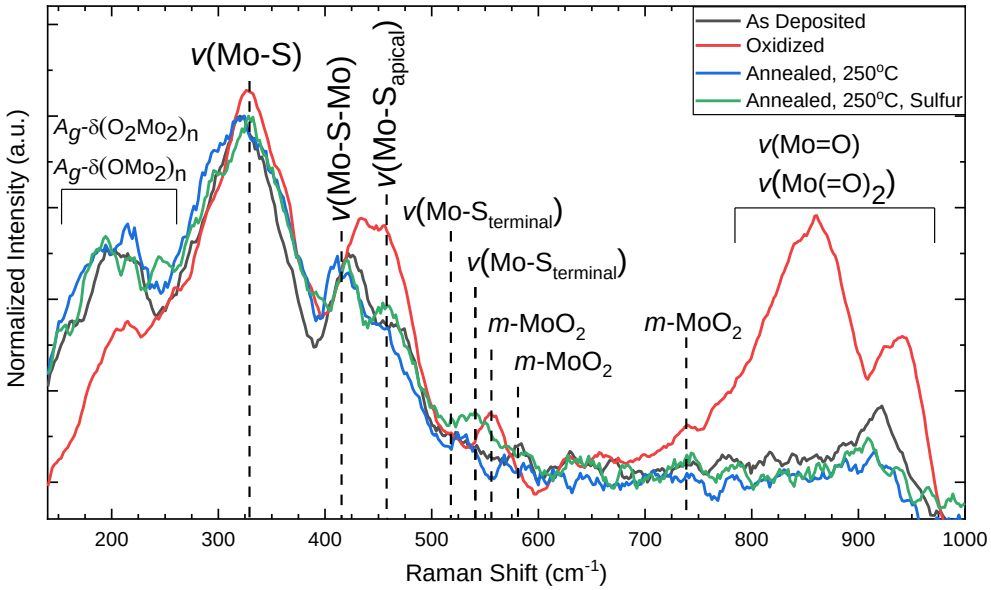

Figure 1: Resonance Raman spectra of MoO_xS_y catalysts

concentration of apical sulfur ligands which is consistent with the XPS findings in Figure 3d. Both annealed samples see an enhancement around 530 cm^{-1}, however it is difficult to attribute this increase to either terminal or bridging ligands with Raman alone.

In order to analyze the chemical states of Mo and S atoms, XPS analysis of the films were performed on each MoO_xS_y catalyst. The XPS of the Mo 3d and S 2p spectra were deconvoluted by fitting the peaks with Voigt functions. The Mo 3d spectra can be deconvoluted into binding energies of four doublets ($3d_{5/2}$ and $3d_{3/2}$) of Mo^{6+}, Mo^{5+}, Mo*, Mo^{4+} and singlets of the various overlapping S 2s states which occur in the same energy range. In Figure 2, as the oxidation number of molybdenum increases in the ascending order of Mo^{4+}, Mo^{*}, Mo^{5+}, and Mo^{6+} ions, with the characteristic doublets being found at higher binding energies which agree with previous literature(*13*, *31*, *44*, *45*). Mo^{4+} is attributed to the Mo center of a-MoS_y, Mo^{5+} is attributed to the Mo center of MoO_xS_y, and Mo^{6+} is attributed to the Mo center of MoO_3. However, to date there has been no report on the intermediate state, Mo^{*}, between Mo^{4+} and Mo^{5+}, which has been observed here. We note that, particularly in Figure 2b, this feature clearly exists even based on visual inspection of the raw data. It is proposed that this peak is associated with an incomplete oxygen replacement of the sulfur ligands. We speculate that this intermediate state is when only one of the sulfur ligands has been replaced by oxygen, resulting in a single bond to the Mo. This would explain the intermediate binding energy found between the Mo^{4+} and Mo^{5+} species.

As seen in Figure 2, the main differences in the chemical state of the catalysts are the oxidation state of molybdenum. In the as deposited sample, the primary molybdenum species present are the Mo^{4+} and Mo^{5+} states with minimal Mo^{6+} as shown in Figure 2a. It is important to note that the Mo^{5+} state is a minor component, or not observed, in electrodeposited MoS_y films when synthesized via $(NH_4)_2MoS_4$. We attribute this large presence of the Mo^{5+} to the dual precursor synthesis approach. However, when exposed to ambient conditions over two days as shown in Figure 2b, the primary species is now the Mo^{6+} state, indicating that the insulating MoO_3 is present, impeding electron transport(*46*). When a freshly deposited sample is annealed under an inert environment, the primary species that are present are the tetravalent state of Mo^{4+} with minimal Mo*, Mo^{5+}, and Mo^{6+}. The freshly deposited sample annealed under a sulfur flux demonstrates similar composition as the sample annealed under an inert environment; however, this has a slightly stronger Mo* peak. Additionally, there are significant changes from the sulfur 2s

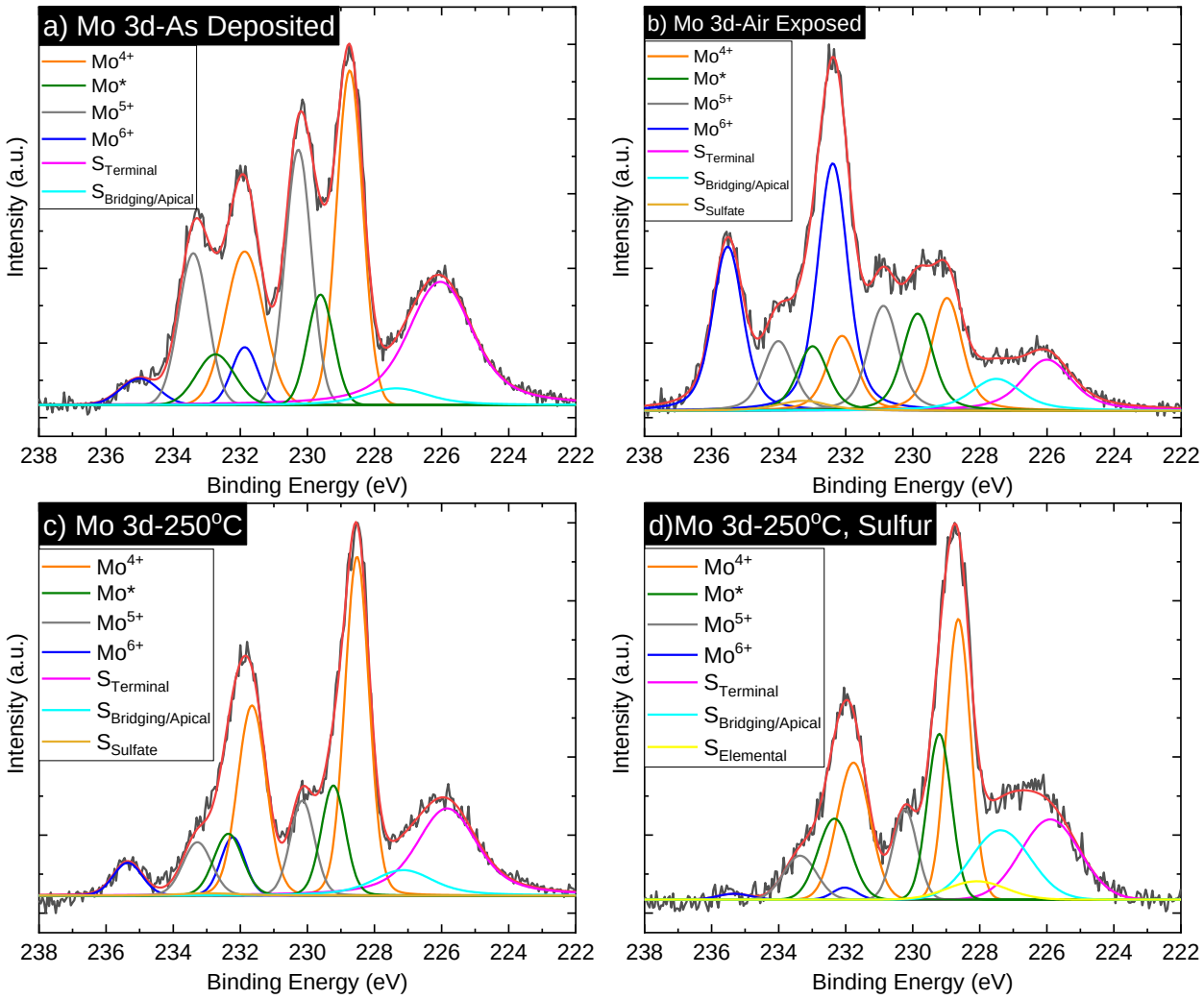

Figure 2: XPS of Mo 3d core electrons of the various MoO_xS_y catalysts

features which will be explained further by analyzing the S 2p peak.

The deconvoluted S 2p spectra consist of four main features of increasing binding energy: (i) terminal S_2^{2-} ligands, (ii) bridging S_2^{2-} and apical S^{2-} ligands, (iii) elemental sulfur, and (iv) sulfates. The as deposited sample is comprised primarily of the S_2^{2-} terminal ligands while after exposure to atmosphere the ratio between the terminal and bridging/apical ligands decreases sharply. This agrees with previous literature, suggesting that the terminal sulfurs are preferentially substituted by oxygen over bridging sulfurs due to a lower thermodynamic barrier(*47*, *48*). The sample annealed under an inert environment maintained similar ratios of terminal to bridging/apical bonds as the freshly deposited sample, while the sample annealed under a sulfur flux demonstrated a decreased ratio of terminal to bridging/apical bonds. This increase in bridging/apical bonds is likely primarily apical sulfur ligands as the associated Raman vibration mode increases as well.

To further examine the impact of the difference in chemical composition on the catalytic properties of the MoO_xS_y catalysts for HER, polarization experiments were performed. The results are shown in **Error! Reference source not found.**. The Tafel slope (b) and the overpotential (η_{10}) required to reach the cathodic current density of 10 mA/cm^2 were used to compare the catalytic activity of the HER catalysts and are shown in Table 1. As it can be seen in **Error! Reference**

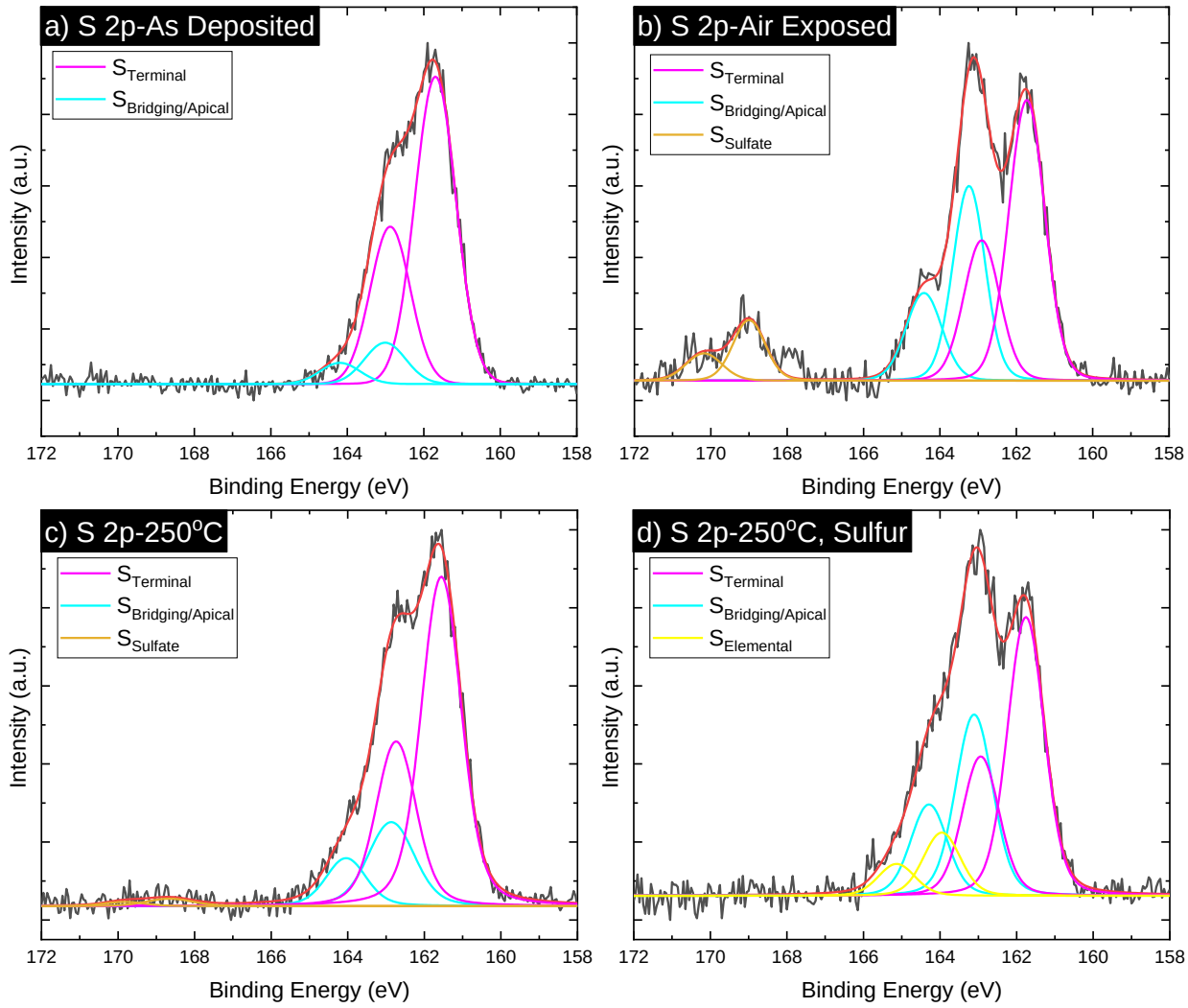

Figure 3: XPS of S 2p core electrons of the various MoO_xS_y catalysts

source not found., the freshly deposited sample performed the best by exhibiting the lowest overpotential (171 mV) of all tested samples. However, when the as deposited film is exposed to ambient conditions for extended periods of time, the activity of the catalyst decreases significantly consistent with previous findings(*37*). Additionally, the performance of the annealed samples became worse, with the sample annealed in the presence of sulfur performing worse than the sample annealed in an inert environment. The sample that was annealed at 450ºC exhibited the worst performance due to its crystalline nature as it was annealed above the crystallization temperature as determined by DSC.

Table 1: Electrochemical measurements of MoO_xS_y catalysts

Sample	η_{10} (mV)	b (mV/dec)
As Deposited	171	74
Oxidized	232	60
Annealed, 250ºC	288	66
Annealed, 250ºC, Sulfur	250	68
Annealed, 450ºC	364	123

The Tafel slope (b), or the slope of the linear, low overpotential regime in the Tafel plot, is the overpotential required to increase the current density by one order of magnitude. Therefore, it is advantageous to have a catalyst with a lower Tafel slope for HER applications. The data shows that

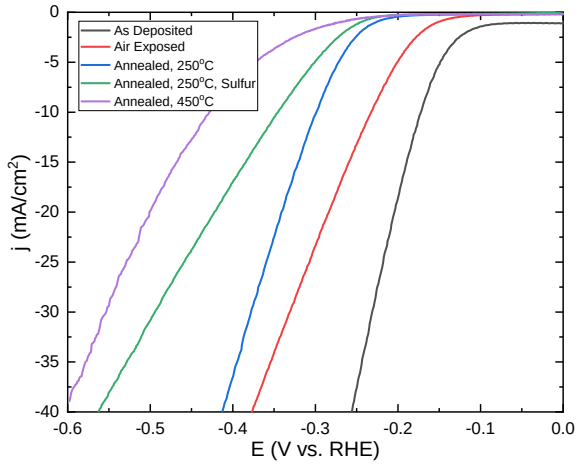

Figure 4: Polarization Curves of MoO_xS_y catalysts

there was little difference between the Tafel slopes of the as deposited sample and oxidized samples, while all annealed samples resulted in slightly lower Tafel slopes. The Tafel slope is dependent on the mechanistic pathway; the HER mechanism involves three known elementary reaction steps in acidic media:

Volmer: $H_3O^+ + e^- \rightarrow H_{ads} + H_2O$

Tafel: $H_{ads} + H_{ads} \rightarrow H_2$

Heyrovsky: $H_{ads} + H_3O^+ + e^- \rightarrow H_2 + H_2O$

Regarding HER, the Volmer reaction will be followed by either the Tafel or Heyrovsky reaction; therefore, there are two possible reaction pathways with those being the Volmer-Tafel and Volmer-Heyrovsky pathways. If the Volmer adsorption reaction is the rate limiting step, a Tafel slop of 120 mV/dec would be expected. If the Tafel or Heyrovsky recombination's are rate limiting, the Tafel slopes would fall between 30 – 40 mV/dec. The Tafel slope for all samples besides the 450^0 C sample laid between these values, suggesting a superposition of mechanisms and therefore mixed kinetics.

As the Raman data demonstrated that the polymeric samples are similar in structure, the chemical composition can be compared to determine its effect on performance. The as deposited sample performed the best out of all tested samples. This can be attributed to the significant presence of Mo^{5+}. As the presence of the Mo^{5+} has been attributed to the two-precursor synthesis route, it can be concluded that this is the primary reason the Levinas study observed superior performance to the single precursor methods. The Mo^{5+} state increases the overall conductivity of the sample but can also act as additional active sites for HER and would explain the superior performance of the MoO_xS_y films(*14*, *49*). However, XPS done following HER shows that the Mo^{5+} state decreased in intensity while the Mo* state increased significantly. This demonstrates the extremely high concentration of Mo^{5+} found in the samples is not completely stable under HER conditions and that the Mo* state might play a significant role in the HER capabilities of the as deposited sample. Additionally, as seen in, the terminal to bridging/apical sulfur ligand ratio decreases slightly, refuting Tran et al. proposed mechanism of the elimination of terminal sulfur ligands and supports Ting et al. breaking of bridging bond generating the catalytic centers for HER(*14*, *36*). The oxidized sample demonstrated poorer performance with respect to the freshly deposited film, as was expected based on Levinas et. al. observations of decreased performance the longer the sample is exposed to the enviroment(*37*). We attribute this decrease in performance to the oxidation of the MoO_xS_y catalyst which can be seen in Figure 2b. The intensity of the Mo^{6+} oxidation state drastically increases with the insulating state of MoO_3 leads to overall worse performance due to reduced electron transfer kinetics. This is supported by the increase in ratio of bridging to terminal sulfur bonds seen in Figure 3b as oxygen will preferentially substitute the terminal sulfur bonds.

The annealed samples showed worse performance compared to the as deposited sample without the presence of the insulating Mo^{6+} state. The sample annealed in the inert environment retained a similar ratio of bridging to terminal sulfur bonds as the freshly deposited sample. However, the inert anneal removed the oxygen dopants associated to the Mo^{5+} as can be seen in Figure 2c. This result emphasizes the importance of oxygen dopants and the Mo^{5+} oxidation state to the overall HER performance. The sample annealed within the

sulfur environment exhibited the worst performance of all polymeric catalysts. This again has been attributed to the loss of incorporated oxygen associated with the Mo^{5+} oxidation state. Additionally, the ratio of bridging/apical to terminal bonds increased substantially. We attribute this observation to the increase of apical bonds instead of bridging bonds as there was an increase in apical sulfur ligands within the Raman spectra. Additionally, it has been reported via quantum chemical simulations that apical bonds are quite inert while bridging bonds are catalytically active(*36*). Those results agree with the findings here in which the increase of apical bonds corresponded to the worse performance of the sulfur annealed film.

Overall, it was shown that the as deposited sample exhibited superior performance due to the presence of the Mo^{5+} oxidation state associated with incorporated oxygen. When left in ambient conditions, the intensity of the insulating Mo^{6+} oxidation increased, leading to decreased performance. The annealing in an inert environment highlighted the importance of the Mo^{5+} oxidation state and that when removed the HER performance suffers. When annealed in a sulfur environment, not only was the Mo^{5+} oxidation state removed, but the concentration of apical sulfur ligands increased substantially, leading to even further reduced HER performance.

4. Results and Discussion – Carbon Tube Synthesis

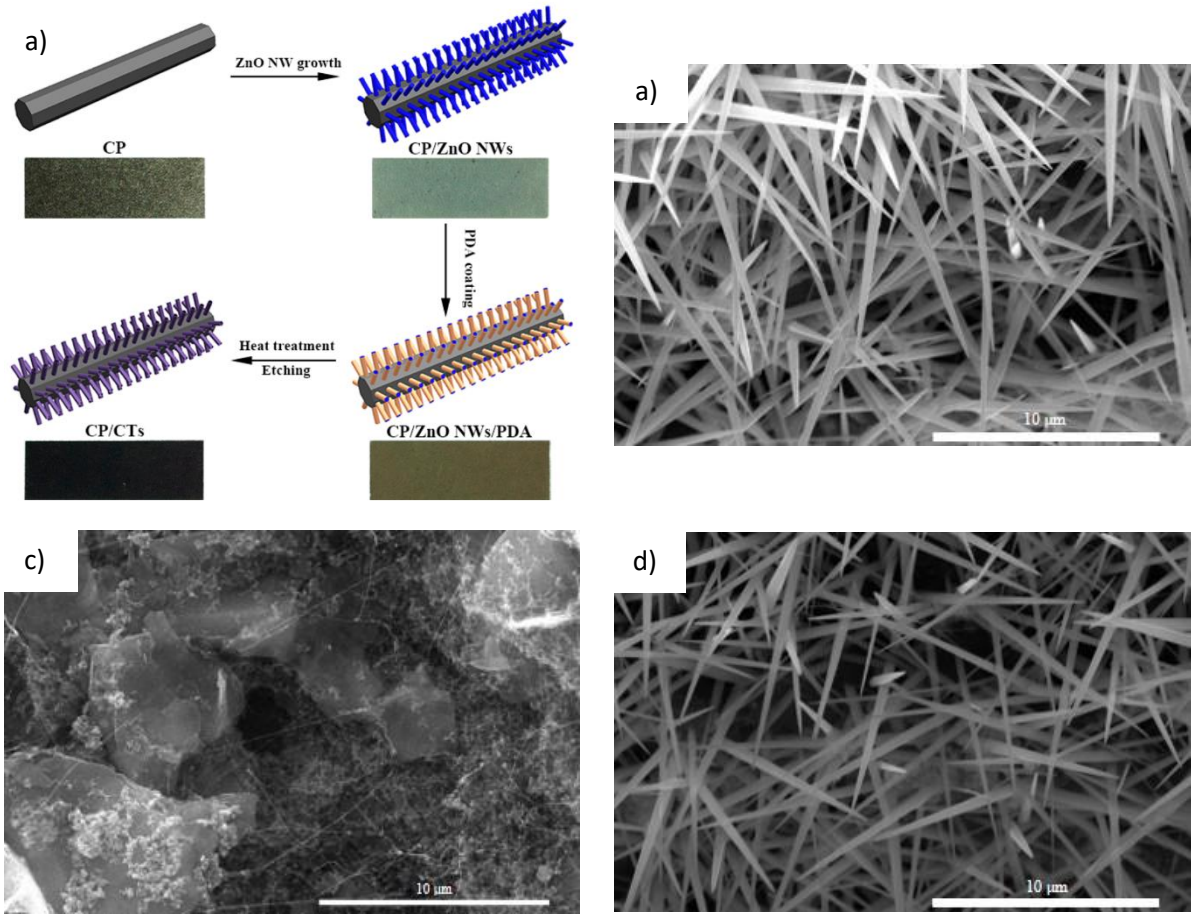

Figure 5: (a) Schematic of synthesis(*38*); SEM images of (b) ZnO NWs, (c) ZnO NWs/PDA after carburizing, and (d) ZnO NWs/PDA

Figure 6 shows the SEM images of the synthesis steps to synthesize the CP/CT substrates. As it can be seen in Figure 6b, the ZnO NWs are densely packed and are uniformly distributed. These NWs possess a high aspect ratio with diameters in the hundreds of nanometers and lengths of several micrometers. Figure 6d reveals that little has changed in the surface morphology of the NWs after PDA coating where we would expect an increase in surface texturing. This suggests that the polymer coating did not successfully adhere to the ZnO NWs. This is further supported by the lack of CTs in Figure 6c. We would expect the same overall structure for the CTs as the ZnO NWs, however after carburizing there is a lack of CTs. As ZnO NWs volatilize at these temperatures whereas CTs do not, this lack of polymer coating is the most likely explanation as to the lack of CTs. As such, we need to continue our investigation of the polymer coating process to elucidate the reasons for the lack of coating. Our early hypothesis is that the addition of Tris in the additionally ethanol is not completely dissolving, therefore not performing its role of a pH buffer on the surface of the ZnO NWs. However, the substrate does show increased performance when MoO_xS_y catalysts are deposited on it over untreated CP and as a film. We have attributed this to the PDA coating the underlying CP fibers and then subsequently being carburized, increasing the overall conductivity. This demonstrates the viability of the 3D substrate and potential, once completely synthesized, to rival the current state-of-the-art catalysts.

5. Conclusions

This study has established the importance of the Mo^{5+} oxidation state arising from oxygen dopants for the HER electrocatalytic performance of MoO_xS_y. When oxygen dopants are removed through annealing, the HER performance of the catalyst is drastically reduced due to the removal of Mo^{5+}. Additionally, this study confirms the hypothesis that oxidation via atmospheric exposure worsens catalytic performance, in line with Levinas et. al. study, due to the presence of Mo^{6+}. The performance difference between the inert and sulfur anneals demonstrated the importance of the terminal and bridging sulfur bonds to the catalytic performance of the MoO_xS_y catalyst and the reduced performance of apical sulfur bonds, confirming quantum chemical simulations(*36*). Finally, this study ascertains the presence of a new Mo chemical state, Mo*, which potentially is critical for the catalytic activity of these films. While the focus of this study was not in determining the origin of this feature, it could lead to future investigations of this chemical state.

To further increase the efficacy of the MoO_xS_y catalysts by increasing the overall conductivity and surface area, a 3D substrate of CTs was employed. Currently, we are unable to successfully synthesize the CTs, but early results have demonstrated the viability of the high surface area, higher conductivity substrate. When successfully synthesized, we believe these catalysts will rival the performance of current state-of-the-art materials while also offering scalable, low-cost synthesis.

References

1. NASA Strategic Plan 2018, pp. 19–21.
2. J. Tsao, N. Lewis, G. Crabtree, *US Dep. Energy*, 1–24 (2006).
3. J. C. Hill, A. T. Landers, J. A. Switzer, *Nat. Mater.* **14**, 1150–1155 (2015).
4. L. Duan, C. M. Araujo, M. S. G. Ahlquist, L. Sun, *Proc. Natl. Acad. Sci. U. S. A.* (2012).
5. V. Kunz *et al.*, *Energy Environ. Sci.* (2017).
6. M. Yoshida, M. Kondo, S. Torii, K. Sakai, S. Masaoka, *Angew. Chemie - Int. Ed.* (2015).
7. M. G. Walter *et al.*, *Chem. Rev.* **110**, 6446–6473 (2010).
8. J. M. Gonçalves, T. A. Matias, K. C. F. Toledo, K. Araki, *Adv. Inorg. Chem.* **74**, 241–303 (2019).
9. A. C. Nielander *et al.*, *Nano Lett.* **16**, 4082–4086 (2016).
10. H. T. Tan, W. Sun, L. Wang, Q. Yan, 2D Transition Metal Oxides/Hydroxides for Energy-Storage Applications. *ChemNanoMat* (2016).

11. R. Rojas Delgado *et al.*, *ACS Appl. Mater. Interfaces*. **9**, 17629–17636 (2017).
12. A. C. Nielander *et al.*, *J. Am. Chem. Soc.* **135**, 17246–17249 (2013).
13. C. G. Morales-Guio, X. Hu, *Acc. Chem. Res.* (2014).
14. P. D. Tran *et al.*, *Nat. Mater.* **15**, 640–646 (2016).
15. Y. Shi, B. Zhang, Recent advances in transition metal phosphide nanomaterials: Synthesis and applications in hydrogen evolution reaction. *Chem. Soc. Rev.* (2016).
16. W. F. Chen, J. T. Muckerman, E. Fujita, *Chem. Commun.* (2013).
17. Y. Wei *et al.*, *Electrochim. Acta* (2019).
18. G. Li *et al.*, *J. Am. Chem. Soc.* (2016).
19. A. Ambrosi, M. Pumera, *ACS Catal.* **6**, 3985–3993 (2016).
20. S. Murugesan *et al.*, *ACS Nano*. **7**, 8199–8205 (2013).
21. T. F. Jaramillo *et al.*, *Science (80-.).* **317**, 100–102 (2007).
22. D. Kong *et al.*, *Nano Lett.* (2013).
23. L. Yang *et al.*, *ACS Nano* (2015).
24. Y. Li *et al.*, *J. Am. Chem. Soc.* **133**, 7296–7299 (2011).
25. S. H. Lin, J. L. Kuo, *Phys. Chem. Chem. Phys.* (2015).
26. J. Lee *et al.*, *J. Phys. Chem. Lett.* (2018).
27. J. Xie *et al.*, *Adv. Mater.* (2013).
28. L. Lin *et al.*, *ACS Nano* (2016).
29. G. Ye *et al.*, *Nano Lett.* (2016).
30. H. Li *et al.*, *Nat. Mater.* (2016).
31. S. Shin *et al.*, *Appl. Surf. Sci.* **487**, 981–989 (2019).
32. J. D. Benck, Z. Chen, L. Y. Kuritzky, A. J. Forman, T. F. Jaramillo, *ACS Catal.* **2**, 1916–1923 (2012).
33. Y. Deng *et al.*, *ACS Catal.* **6**, 7790–7798 (2016).
34. T. Weber, J. C. Muijsers, J. W. Niemantsverdriet, *J. Phys. Chem.* (1995).
35. S. J. Hibble, D. A. Rice, D. M. Pickup, M. P. Beer, *Inorg. Chem.* (1995).
36. L. R. L. Ting *et al.*, *ACS Catal.* (2016).
37. R. Levinas, N. Tsyntsaru, H. Cesiulis, *Electrochim. Acta*. **317**, 427–436 (2019).
38. J. Wang, H. X. Zhong, Z. L. Wang, F. L. Meng, X. B. Zhang, *ACS Nano*. **10**, 2342–2348 (2016).
39. J. Kibsgaard, T. F. Jaramillo, F. Besenbacher, *Nat. Chem.* **6**, 248–253 (2014).
40. M. A. Camacho-López *et al.*, *Opt. Mater. (Amst).* (2011).
41. C. H. Chang, S. S. Chan, *J. Catal.* (1981).
42. A. Müller, V. Wittneben, E. Krickemeyer, H. Bögge, M. Lemke, *ZAAC - J. Inorg. Gen. Chem.* (1991).
43. V. P. Fedin, B. A. Kolesov, Y. V. Mironov, V. Y. Fedorov, *Polyhedron* (1989).
44. H. Vrubel, X. Hu, *ACS Catal.* **3**, 2002–2011 (2013).
45. D. Bélanger, G. Laperrière, F. Girard, D. Guay, G. Tourillon, *Chem. Mater.* (1993).
46. C. Zhang, L. Jiang, Y. Zhang, J. Hu, M. K. H. Leung, *J. Catal.* (2018).
47. J. Martincová, M. Otyepka, P. Lazar, *Chem. - A Eur. J.* **23**, 13233–13239 (2017).
48. J. Gao *et al.*, *ACS Nano* (2016).
49. E. Schmidt, C. Sourisseau, G. Meunier, A. Levasseur, *Thin Solid Films* (1995).